Coronal Microjets in Quiet-Sun Regions Observed with the Extreme Ultraviolet Imager on Board the Solar Orbiter

Zhenyong Hou[1] , Hui Tian[1,2] , David Berghmans[3], Hechao Chen[1] , Luca Teriaca[4], Udo Schühle[4], Yuhang Gao[1],
Yajie Chen[1] , Jiansen He[1] , Linghua Wang[1] , and Xianyong Bai[2]

[1] School of Earth and Space Sciences, Peking University, Beijing, 100871, People's Republic of China; huitian@pku.edu.cn
[2] Key Laboratory of Solar Activity, National Astronomical Observatories, Chinese Academy of Sciences, Beijing, 100012, People's Republic of China
[3] Solar-Terrestrial Centre of Excellence − SIDC, Royal Observatory of Belgium, Ringlaan -3- Av. Circulaire, 1180 Brussels, Belgium
[4] Max-Planck-Institut für Sonnensystemforschung, Göttingen, Germany

Abstract

We report the smallest coronal jets ever observed in the quiet Sun with recent high-resolution observations from the High Resolution Telescopes (HRI_{EUV} and $HRI_{Ly\alpha}$) of the Extreme Ultraviolet Imager on board the Solar Orbiter (SO). In the HRI_{EUV} (174 Å) images, these microjets usually appear as nearly collimated structures with brightenings at their footpoints. Their average lifetime, projected speed, width, and maximum length are 4.6 minutes, 62 km s^{-1}, 1.0 Mm, and 7.7 Mm, respectively. Inverted-Y shaped structures and moving blobs can be identified in some events. A subset of these events also reveal signatures in the $HRI_{Ly\alpha}$ (H I Lyα at 1216 Å) images and the extreme ultraviolet images taken by the Atmospheric Imaging Assembly (AIA) on board the Solar Dynamics Observatory (SDO). Our differential emission-measure (EM) analysis suggests a multithermal nature and an average density of $\sim 1.4 \times 10^9$ cm^{-3} for these microjets. Their thermal and kinetic energies were estimated to be $\sim 3.9 \times 10^{24}$ erg and $\sim 2.9 \times 10^{23}$ erg, respectively, which are of the same order of the released energy predicted by the nanoflare theory. Most events appear to be located at the edges of network lanes and magnetic flux concentrations, suggesting that these coronal microjets are likely generated by magnetic reconnection between small-scale magnetic loops and the adjacent network field.

Unified Astronomy Thesaurus concepts: Quiet sun (1322); Solar ultraviolet emission (1533); Solar corona (1483)

Supporting material: animation

1. Introduction

Solar jets are one type of pervasive and explosive phenomena on the Sun, usually appearing as a footpoint brightening followed by a nearly collimated plasma ejection (e.g., Raouafi et al. 2016; Zheng et al. 2018; Shen 2021). Coronal jets are often observed in extreme ultraviolet (EUV; e.g., Nisticò et al. 2009; Yang et al. 2011; Srivastava et al. 2012; Chandrashekhar et al. 2014b; Kumar et al. 2018, 2019a, 2019b) and X-ray passbands (e.g., Shimojo et al. 1996; Sterling et al. 2019) in active regions (ARs) and coronal holes. These coronal jets normally appear as anemone jets (i.e., inverted-Y or λ shape, e.g., Cirtain et al. 2007; Nisticò et al. 2009) or two-sided-loop jets (e.g., Tian et al. 2017; Wei et al. 2020). The anemone jets can be divided into blowout jets and standard jets (e.g., Moore et al. 2010). The obvious differences are that a blowout jet often hosts two bright points (only one bright point at a standard one's base) and often involves a twisting mini-filament at its base (Moore et al. 2010; Sterling et al. 2015; Zhu et al. 2017; Moore et al. 2018; Yang et al. 2019). Observational studies show that the coronal jets are often associated with or occur above satellite sunspots (Chen et al. 2008, 2015; Sakaue et al. 2017; Shen et al. 2018; Paraschiv et al. 2020), coronal bright points (CBPs; Culhane et al. 2007; Li et al. 2016; Madjarska 2019), mini-filaments (Hong et al. 2016; Sterling et al. 2016; Kumar et al. 2018, 2019b), or sigmoidal structures (Chandrashekhar et al. 2014a; Liu et al. 2016). Coronal jets have been frequently found to be closely related to flux emergence, flux convergence, and/or cancellation, indicating their generation by magnetic reconnection (Jiang et al. 2007; He et al. 2010; Shen et al. 2012;

Panesar et al. 2016). The brightening of the loops at the bases of some jets is found to be associated with a pattern of Doppler blue-to-redshifts, indicating an outbreak of siphon flow along the newly reconnected and submerging closed loop during the interchange magnetic reconnection (He et al. 2010). The lengths, widths, projected speeds, lifetimes, temperatures, and densities of coronal jets are mostly 10–400 Mm, 5–100 Mm, 10–1000 km s^{-1}, tens of minutes, 3–8 MK, and 0.7–4.0×10^9 cm^{-3}, respectively (Shimojo & Shibata 2000; Savcheva et al. 2007; Paraschiv et al. 2015; Mulay et al. 2016; Panesar et al. 2018).

Jet-like features have also been observed in the chromosphere and transition region (TR). These low-temperature jets are usually smaller than the coronal jets, and they appear as anemone jets in plage regions (e.g., Shibata et al. 2007; Wang et al. 2021), penumbral jets (e.g., Katsukawa et al. 2007; Tiwari et al. 2016; Hou et al. 2020), light bridge jets (e.g., Bharti et al. 2017; Hou et al. 2017; Tian et al. 2018; Bai et al. 2019), flare ribbon jets (Li et al. 2019), cool polar jets (Srivastava & Murawski 2011), mini- or nano-jets from rotating prominence structures (Chen et al. 2017a; Antolin et al. 2021), chromospheric spicules (e.g., de Pontieu et al. 2007; Rouppe van der Voort et al. 2015; Samanta et al. 2019), TR network jets (e.g., Tian et al. 2014b; Narang et al. 2016; Chen et al. 2019; Qi et al. 2019), and TR explosive events (TREEs) interpreted as bidirectional jets (Innes et al. 1997). Though smaller in size, many chromospheric/TR jets have morphologies that are similar to those of coronal jets. For instance, many of these small jets also reveal inverted-Y-shaped structures, indicating that magnetic reconnection between small-scale magnetic loops and the background field might be a common formation

Table 1
Detailed Information of the EUI Data Sets

Data Set	Date	Time (UT)	Distance from Sun (AU)	Pixel Size $\mathrm{HRI_{EUV}}$ ($\mathrm{HRI_{Ly\alpha}}$) (Mm)	Time Cadence (s)	Lyα Data Available?	SDO Data Available?
1	2020-05-20	21:12–22:09	0.61	0.22 (/)	10	/	yes
2	2020-05-21	16:04–17:30	0.60	0.22 (/)	10 (60)	/	yes
3	2020-05-30	14:46–14:50	0.56	0.19 (0.21)	5	yes	yes
4	2020-10-19	19:44–20:31	0.99	0.35 (/)	12	/	/
5	2020-10-22	14:23–14:36	0.98	0.35 (/)	10	/	/
6	2020-11-19	11:52–14:31	0.92	0.32 (0.68)	15	yes	/

Note. For data set 2, the regular time cadence is 10 s covering most microjets, whereas the time cadence of 60 s covers two microjets (Jet-09 and Jet-12). For data set 6, the $\mathrm{HRI_{Ly\alpha}}$ images were binned with 2×2 pixels.

mechanism for these jets (e.g., Ni et al. 2020). The lengths, widths, velocities, and lifetimes of these chromospheric/ TR jets have been found to be 1–11 Mm, 100–400 km, 5–250 km s^{-1}, and 20–500 s, respectively. Due to their high occurrence rate and ubiquity, these small-scale jets have been suggested to contribute significantly to the heating of the upper solar atmosphere and origin of the solar wind (e.g., De Pontieu et al. 2011; Tian et al. 2014b; Samanta et al. 2019).

With recent high-resolution observations taken by the Extreme Ultraviolet Imager (EUI; Rochus et al. 2020) on board the Solar Orbiter (SO; Müller et al. 2020), we report the smallest coronal jets ever observed in the quiet Sun and investigate their physical properties. We describe our observations in Section 2, present the analysis results in Section 3, discuss the results in Section 4, and summarize our findings in Section 5.

2. Observations

The primary data[5] that we used were taken by the two High Resolution Imagers (HRI) of EUI, the passbands of which are centered at 174 Å ($\mathrm{HRI_{EUV}}$: dominated by Fe X and Fe IX lines) and 1216 Å ($\mathrm{HRI_{Ly\alpha}}$: dominated by the Lyα line of hydrogen), respectively (Berghmans et al. 2021). The $\mathrm{HRI_{EUV}}$ passband has a peak response at the temperature of ∼1 MK (Chen et al. 2021), and thus samples plasma in the corona. We mainly used $\mathrm{HRI_{EUV}}$ images to search for coronal microjets. Six data sets taken on 2020 May 20, May 21, May 30, October 19, October 22, and November 19 were analyzed. The detailed information of these data sets is shown in Table 1.

We also analyzed simultaneous observations taken by the Atmospheric Imaging Assembly (AIA; Lemen et al. 2012) and the Helioseismic and Magnetic Imager (HMI; Scherrer et al. 2012) on board the Solar Dynamics Observatory (SDO; Pesnell et al. 2012) on 2020 May 20, May 21, and May 30, when the field of views (FOVs) of EUI HRIs were also seen by SDO. We used the AIA 1600 Å images at a 24 s cadence and the 304, 171, 193, 211, 131, 335, and 94 Å images at a 12 s cadence to investigate the thermal property of the coronal microjets. These AIA images have a pixel size of 430 km and a resolution of about 1 Mm. To investigate their origin, we also examined the HMI line-of-sight (LOS) magnetic field data at a 45 s cadence. The pixel size of the magnetograms is 360 km.

Because the $\mathrm{HRI_{EUV}}$ and the AIA 171 Å images have similar temperature responses, we first aligned them through a linear Pearson correlation. And other AIA and HMI images were then aligned with the AIA 171 Å images using the aia_prep.pro

routine available in SolarSoftware. For aligning the $\mathrm{HRI_{EUV}}$ and $\mathrm{HRI_{Ly\alpha}}$ images, several CBPs in the images were used as the referent features. Due to the difference in the heliocentric distance of SO and SDO, the solar radiation emitted at a particular time reaches the two spacecraft at different times. To avoid confusion in further analysis, we converted the observation times of all telescopes into the light-emitting times on the Sun, which are listed in Table 1.

3. Results

Figure 1 shows an overview for each of the six data sets in the $\mathrm{HRI_{EUV}}$ passband. The Sun was very quiet on these days, and the FOVs mainly include wide-spreading CBPs and diffuse regions in between. Several ARs appear near the edges of the FOVs in data sets 4–6; these ARs were saturated due to their high radiance and were excluded when searching for coronal jets. The high spatial and temporal resolutions allow us to investigate various types of small-scale transient activity. Previous investigations have identified numerous small brightenings called "campfires" from these $\mathrm{HRI_{EUV}}$ images (Berghmans et al. 2021). Here we focus on small-scale collimated jet-like features, which we call "coronal microjets."

In total, we identified 52 coronal microjets from the six $\mathrm{HRI_{EUV}}$ image sequences. The footpoint locations of all these jets are marked in Figure 1. The detailed information such as the staring times of their occurrence on the Sun, durations, and pixel locations are listed in Table 2. There are two events in each of the data sets 1, 3 and 5, 11 events in data set 2, 7 events in data set 4, and 27 events in data set 6. Figure 1 shows that most of these microjets are located in the quiet-Sun regions that are far away from the ARs. A few of them are located close to but not inside the ARs.

3.1. Morphology and Parameters of the Coronal Microjets in $\mathrm{HRI_{EUV}}$

The identified microjets are generally preceded by clear brightenings at their footpoints in the $\mathrm{HRI_{EUV}}$ images. They mostly appear as collimated structures shooting up from the footpoint brightenings. Their morphology is very similar to the known larger-scale coronal jets. As an example, we show six coronal microjets in Figure 2.

Figure 2(a) gives a closer look at Jet-04. To highlight the jet, we manually drew a green contour enclosing the jet structure. The green arrow indicates the propagation direction of the jet. This jet appears to consist of two footpoints and a collimated jet body, forming an inverted-Y-shaped structure. Figure 2(b) gives a closer look at Jet-17. In addition to the two footpoints at
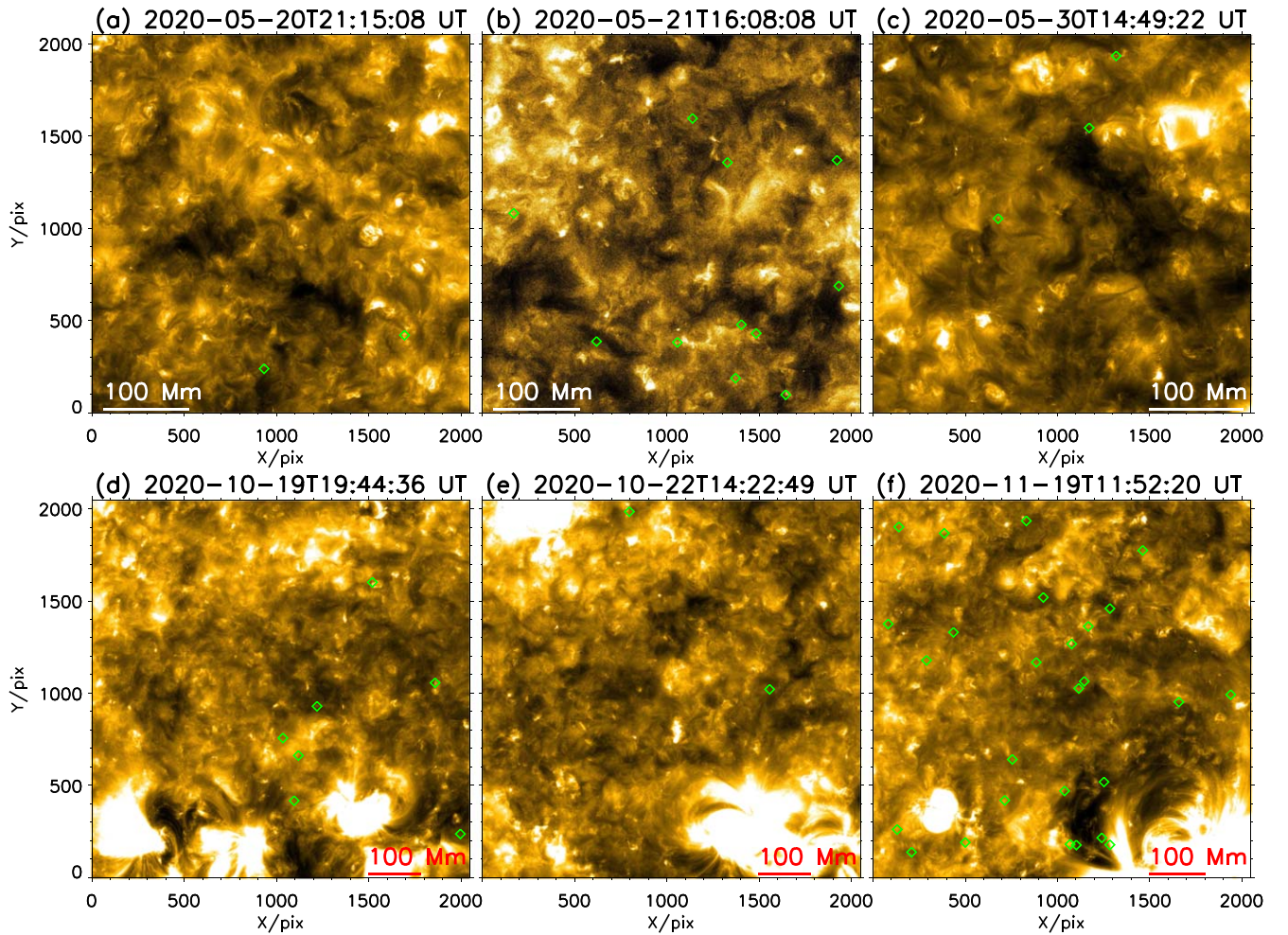
Figure 1. Overviews for all the six data sets in the HRI$_{EUV}$ passband. The green open diamond in each panel mark the footpoint locations of the identified coronal microjets.

the base and the quasi-collimated jet body, two blobs marked by the red arrows in Figure 2(b) can be clearly seen in the jet. These moving blobs appear to be similar to those reported in large-scale coronal jets (Zhang & Ji 2014; Zhang et al. 2016; Kumar et al. 2018, 2019a, 2019b). Two blobs can also be identified from Jet-35, as marked by the red arrows in Figure 2(c). For a detailed evolution of these moving blobs, we refer to the associated animation of Figure 2. The jet shown in Figure 2(d) (Jet-07) is a highly collimated one. It includes a brighter, confined base and a fuzzy but identifiable jet body. Figure 2(e) shows a bidirectional jet (Jet-20). We see that plasma is ejected toward the opposite directions from the jet base, which is marked by the plus symbol. The last example is Jet-50, shown in Figure 2(f). Two microjets occur close to each other simultaneously. The footpoints of these two jets appear to be kinked or reveal two branches, possibly indicating an inverted-Y-shape morphology. From the associated animation, we can see the appearance of two dark regions following the disappearance of Jet-50, which might be similar to the coronal dimmings after eruptions of coronal mass ejections (e.g., Sterling & Hudson 1997; Xing et al. 2020). Moreover, from Figure 2 and the associated animation we see that most microjets appear as isolated structures without any indication of pre-eruption mini-filaments at their bases, which is different

from many previously reported coronal jets in ARs and coronal holes.

We measured the physical parameters for these coronal microjets, i.e., the duration, projected speed, length, width, and aspect ratio, which are listed in Table 2. The lifetime of each event was calculated as the time difference between the first appearance of the footpoint brightening and the disappearance of the jet body. For several events either the first appearance of the footpoint brightening or the disappearance of the jet body was not captured by EUI, we thus cannot accurately estimate their full lifetimes. Instead, we registered the existing periods of these jets in the HRI$_{EUV}$ images (see Table 2). We marked the trajectory of each microjet and calculated the speed from the corresponding time–distance map. As an example, Figures 3(a) and (b) show the trajectory and the time–distance map for Jet-14, respectively. Four slant stripes, marking four episodes of plasma ejection in Jet-14, can be seen from Figure 3(b). The speeds for the four ejections were estimated from the slopes, which range from 89 to 162 km s^{-1}. We took the average speed 123 km s^{-1} as the speed of this jet for further analysis. We would like to mention that most microjets only show one episode of ejection, and in such cases there is no need to average the speeds. We calculated the length of a microjet when it was fully developed and clearly resolved. To estimate

Table 2
Detailed Information of the Coronal Microjets

Jet ID	Date 2020-	ST (UT)	Duration (s)	Location X/Y	Speed (km s^{-1})	Length (Mm)	Width (Mm)	Lyα	AIA	OP	Lane	Log (Ne) (cm^{-3})
01	05–20	22:03:08	>530	932/238	46	/	/	/	yes	yes	yes	9.15
02	05–20	21:15:48	370	1693/420	46	5.3	0.7	/	yes	yes	yes	9.15
03	05–21	16:10:38	>305	618/386	69	10.0	1.2	/	weak	yes	yes	/
04	05–21	16:10:08	60	1483/430	52	4.0	0.4	/	yes	yes	yes	9.35
05	05–21	16:42:38	180	1056/381	41	2.7	0.5	/	yes	yes	yes	9.15
06	05–21	16:40:58	50	1643/97	50	2.0	0.4	/	yes	yes	yes	9.17
07	05–21	16:43:58	190	1931/687	111	7.9	1.0	/	yes	maybe	yes	9.03
08	05–21	17:03:13	165	1403/477	71	4.2	0.5	/	yes	yes	close	9.15
09	05–21	17:11:58	300	1371/187	29	4.2	1.0	/	yes	maybe	yes	9.03
10	05–21	16:45:38	80	1327/1356	75	4.8	0.4	/	yes	no	no	9.20
11	05–21	16:42:58	230	1138/1595	179	9.4	0.9	/	weak	yes	yes	/
12	05–21	17:20:58	180	169/1081	30	8.1	0.6	/	yes	yes	yes	9.26
13	05–21	16:59:58	210	1921/1368	59	6.5	1.0	/	weak	yes	close	/
14	05–30	14:50:58	80	678/1052	123	5.4	0.7	yes	yes	maybe	yes	9.15
15	05–30	14:51:38	45	1172/1544	72	2.8	0.5	no	no	no	yes	/
16	05–30	14:49:22	>96	1318/1934	43	2.9	0.6	no	yes	maybe	yes	9.24
17	10–19	20:02:48	564	1095/417	70	12.4	1.1	/	/	/	/	/
18	10–19	20:21:12	300	1118/662	43	11.7	2.9	/	/	/	/	/
19	10–19	20:15:12	300	1034/757	84	5.7	1.0	/	/	/	/	/
20	10–19	20:00:41	199	1996/237	130	8.6	1.2	/	/	/	/	/
21	10–19	19:59:36	576	1219/929	41	7.5	1.6	/	/	/	/	/
22	10–19	20:22:36	84	1859/1056	132	6.5	0.7	/	/	/	/	/
23	10–19	20:28:00	>204	1519/1601	87	5.4	1.0	/	/	/	/	/
24	10–22	14:25:49	160	1556/1021	69	3.4	0.8	/	/	/	/	/
25	10–22	14:27:39	>540	796/1984	77	9.5	2.7	/	/	/	/	/
26	11–19	11:55:35	225	209/138	65	5.7	0.8	no	/	/	yes	/
27	11–19	13:03:21	540	500/191	74	7.8	1.3	no	/	/	yes	/
28	11–19	14:07:51	135	131/261	77	6.1	0.8	/	/	/	/	/
29	11–19	12:19:51	420	714/419	36	7.4	1.6	no	/	/	yes	/
30	11–19	13:19:06	270	755/641	61	4.7	1.1	yes	/	/	yes	/
31	11–19	12:10:21	225	1068/181	56	6.3	0.9	no	/	/	yes	/
32	11–19	13:53:36	615	1240/216	48	20.0	1.7	yes	/	/	yes	/
33	11–19	13:58:51	405	1284/178	60	4.1	0.8	no	/	/	yes	/
34	11–19	12:05:20	271	1038/470	45	5.2	1.3	yes	/	/	yes	/
35	11–19	14:23:51	>495	1252/519	18	7.2	0.8	no	/	/	yes	/
36	11–19	13:54:06	455	290/1178	24	6.5	0.8	yes	/	/	yes	/
37	11–19	14:19:51	150	885/1167	54	5.2	1.1	yes	/	/	yes	/
38	11–19	13:29:36	150	1145/1064	106	5.2	0.8	no	/	/	yes	/
39	11–19	13:57:51	180	1115/1026	65	6.6	0.9	no	/	/	yes	/
40	11–19	12:05:20	256	1658/952	39	4.1	0.9	yes	/	/	yes	/
41	11–19	12:20:36	255	1939/992	42	6.2	1.0	no	/	/	yes	/
42	11–19	14:18:21	150	82/1375	38	6.7	0.7	/	/	/	/	/
43	11–19	12:55:06	>2085	436/1330	30	23.4	1.2	no	/	/	no	/
44	11–19	13:52:21	330	923/1519	41	7.3	1.5	no	/	/	yes	/
45	11–19	13:18:06	315	1167/1362	44	9.8	1.4	yes	/	/	yes	/
46	11–19	14:04:51	675	1284/1459	96	15.6	1.2	yes	/	/	yes	/
47	11–19	13:01:51	270	386/1867	34	13.5	1.1	yes	/	/	yes	/
48	11–19	13:55:36	240	140/1901	27	13.3	1.8	/	/	/	/	/
49	11–19	13:16:06	525	831/1934	38	10.3	1.5	no	/	/	yes	/
50	11–19	14:07:51	465	1462/1774	47	9.2	1.0	yes	/	/	yes	/
51	11–19	11:54:50	225	1077/1267	85	15.5	1.2	no	/	/	yes	/
52	11–19	12:30:36	>90	1102/177	63	8.4	0.8	no	/	/	yes	/

Note. ST: the starting time of one microjet on the Sun, inferred from the HRI$_{\rm EUV}$ images. Location: the location of a microjet in the pixel coordinate of a HRI$_{\rm EUV}$ image. Lyα: if a microjet reveals a signature in the HRI$_{\rm Ly\alpha}$ images. AIA: if a microjet reveals a signature in AIA EUV images. OP: if a microjet is associated with opposite magnetic polarities. Lane: if a microjet originates from the network lane. Jet-01 is a complex event, including several microjet-like structures that appear simultaneously at two adjacent locations. Therefore, it is difficult to estimate a length and a width. The projected speed was calculated from the AIA 171 Å images.

the width of a microjet, we put a narrow white rectangle perpendicular to the microjet, as exemplified in Figure 3(a). We then plotted the intensity along the long side of the rectangle and obtained the intensity profile across the jet, e.g., the black line in Figure 3(c). We applied a Gaussian fit to the intensity profile, and the FWHM was taken as the width of the microjet.
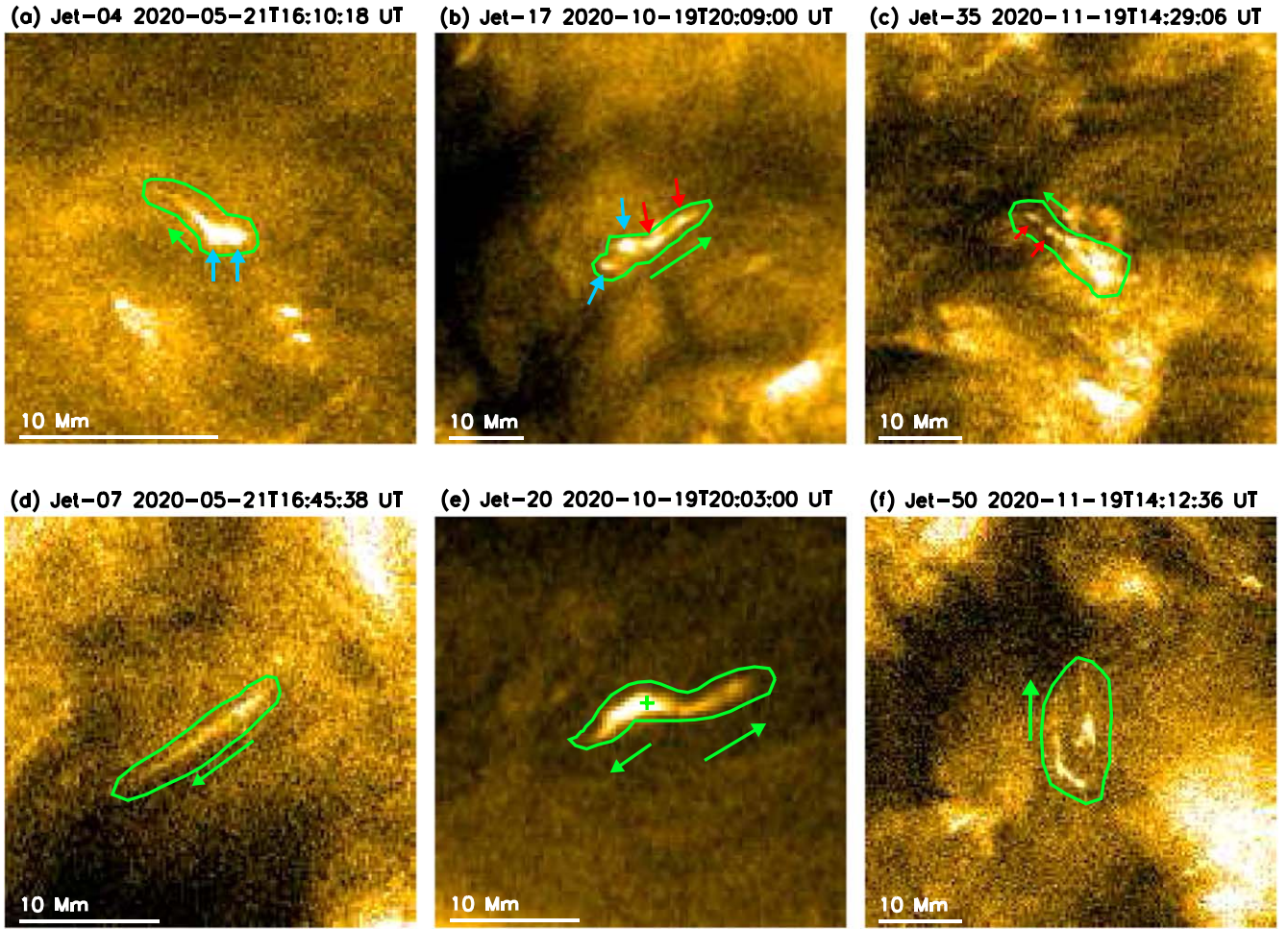
Figure 2. Morphologies of Jet-04, Jet-17, Jet-35, Jet-07, Jet-20, and Jet-50 in the HRI$_{EUV}$ images. The green contours outline the microjets, and the green arrows indicate the propagation directions of the microjets. In (a) and (b), the blue arrows mark the footpoints of the microjets. In (b) and (c), the red arrows indicate some blobs within the microjets. In (e), the green plus marks the location of the starting brightening in Jet-20. An animation of this figure is available, showing the evolution of these six microjets in the HRI$_{EUV}$ images. It includes six panels covering durations of 2 minutes from 16:09:38 UT to 16:11:38 UT on 2020 May 21, 10.6 minutes from 20:02:24 UT to 20:13:00 UT on 2020 October 19, 8.3 minutes from 14:23:51 UT to 14:32:06 UT on 2020 November 19, 5.7 minutes from 16:41:28 UT to 16:47:08 UT on 2020 May 21, 3.3 minutes from 20:00:41 UT to 20:04:00 UT on 2020 October 19, and 7.8 minutes from 14:07:51 UT to 14:15:36 UT on 2020 November 19, respectively. In this animation, the green arrows mark the microjets, the red arrows in (b) and (c) mark the blobs, and the white arrows in (f) denote two dark regions that appear after the disappearance of Jet-50.

(An animation of this figure is available.)

Finally, the aspect ratio of the microjet could be calculated as the ratio of the length and width.

Figures 3(d)−(h) show the distributions of their parameters. Their durations are shorter than 11 minutes, with an average of ∼4.6 minutes in length. Their projected speeds are mostly less than 100 km s^{-1} with an average value of ∼62 km s^{-1}. These microjets have lengths ranging from 2 to 20 Mm, with an average of ∼7.7 Mm. Their widths, obtained as the FWHM of a Gaussian function fitted to the intensity profile, are in the range of 0.3–3.0 Mm, and the average value is ∼1.0 Mm. The aspect ratios of the microjets range from 3 to 20, and the average is 7.7.

3.2. Response in the HRI$_{Ly\alpha}$ Images

We also examined responses of the identified coronal microjets in the HRI$_{Ly\alpha}$ images. Data sets 3 (three events) and 6 (27 events) have simultaneous observations in the HRI$_{Ly\alpha}$ passband. We found that 11 out of the 30 jets (see the details in Table 2) have emission responses at the jet locations in the HRI$_{Ly\alpha}$ images, and three examples are shown in Figure 4. We chose one region around the footpoint of each

microjet (red contours in the left and middle columns of Figure 4) and plotted the light curves of the total intensities at 174 Å and H I Lyα in the right column of Figure 4. The two light curves reveal a similar trend for these three microjets, indicating that emissions in the two passbands are mainly contributed by the same process. These microjets with clear response in Lyα might be generated at lower heights as compared to others.

By comparing the left and middle columns of Figure 4, we can see that these microjets are located at or near the network lanes that are characterized by the enhanced emission in the HRI$_{Ly\alpha}$ images. Actually, at least half of the 30 microjets (including the three microjets shown in Figure 4) appear to be located at the edges of the network lanes. Only one microjet (Jet-43, see Table 2) is not near the network lane.

3.3. Response in the AIA Images and the Associated Magnetic Field

The FOVs of data sets 1 (two events), 2 (11 events), and 3 (three events) have also been observed by AIA and HMI. We
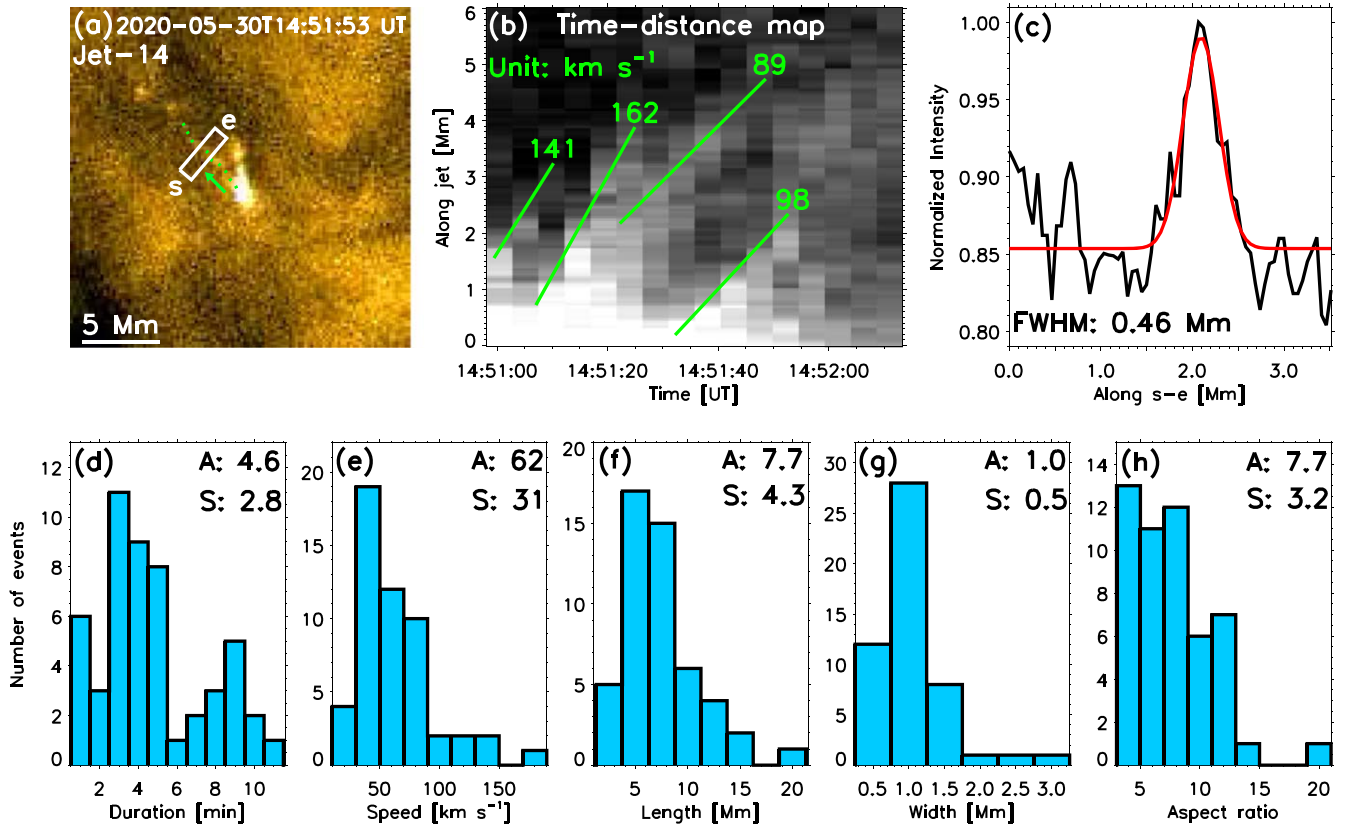
Figure 3. Parameters of the coronal microjets. (a) An HRI$_{EUV}$ image showing Jet-14 at 14:51:35 UT on 2020 May 30. The green arrow indicates the propagation direction, and the green dotted line marks the trajectory of the ejected plasma. (b) The time–distance map for the green dotted line in (a). Four tracks of ejected plasma and the corresponding projected speeds in the unit of km s^{-1} are marked by the green lines and the numbers, respectively. (c) The intensity variation along the long side of the rectangle s−e shown in (a). The original intensity profile and the Gaussian fit are indicated by the black and red curves, respectively. (d)−(h) Distributions of the parameters for the microjets. In each panel, "A" and "S" represent the average value and standard deviation, respectively.

thus examined the responses of these events in the AIA ultraviolet (UV) and EUV images, and investigated the possible origin of these jets using the HMI LOS magnetograms. We did not find any signature of these events in the AIA 1600 Å images. Many microjets reveal obvious signatures in the AIA 304, 171, 193, and 211 Å passbands, and for some cases weak signatures can be identified from the AIA 335 and 131 Å passbands (Table 2). As an example, Figure 5 shows two events, Jet-02 and Jet-04, in the HRI$_{EUV}$, AIA 171, and 211 Å images. These two events reveal clear signatures in the AIA 171 and 211 Å images, especially around their footpoint regions. The jet signatures are fuzzier in the AIA EUV passbands than in the HRI$_{EUV}$ images. Without the high-resolution HRI$_{EUV}$ observations, it would be difficult to identify these coronal microjets from the AIA EUV passbands.

With the HMI magnetograms, we have examined the magnetic field structures around the coronal microjets. We found that 10 events are located in regions with opposite magnetic polarities (see the details in Table 2). In Figures 5(a4) and (b4), we show the LOS magnetic field around Jet-02 and Jet-04. Jet-02 is obviously located above a region with opposite polarities, where the negative polarity is dominated. The footpoint region of Jet-04 is also a mixed-polarity region, where a weak negative flux is close to the strong positive flux of the network. In some cases, there are more than one patches of the minor polarity around their footpoints. These events were also considered to be related to opposite-polarity fluxes if

one patch consists of more than 4 pixels with a field strength larger than 10 G.

The resolution of the HMI magnetograms is not high enough to reveal clear flux changes of the magnetic field associated with most of the microjets. However, we did find clear magnetic flux changes for a few microjets. We present the variations of the minority-polarity magnetic fluxes for two events in Figures 5(a4) and (b4), where we can see clear signatures of flux decrease between the starting and ending times of each event. In addition, the positive magnetic flux (not shown in Figure 5(b4)) associated with Jet-04 reveals an obvious decrease during the occurrence of the jet, similar to the negative flux. Magnetic cancellation is also associated with some coronal jets (e.g., Chen et al. 2015, 2017b). These observational signatures indicate that magnetic cancellation is likely associated with at least some microjets.

Using the co-aligned AIA 1600 Å images and HMI magnetograms, we can also find that almost all of the 16 microjets identified from data sets 1, 2, and 3 originate from the bright network lanes or the relatively strong magnetic flux concentrations. The footpoints of some microjets are clearly located at the edges of magnetic flux concentrations. As mentioned above, a similar result was also found from the HRI$_{Ly\alpha}$ images (see the details in Table 2).

3.4. Differential Emission-measure (DEM) Analysis

For the coronal microjets observed in 2020 May (except Jet-15 without emission response in the AIA EUV passbands), we
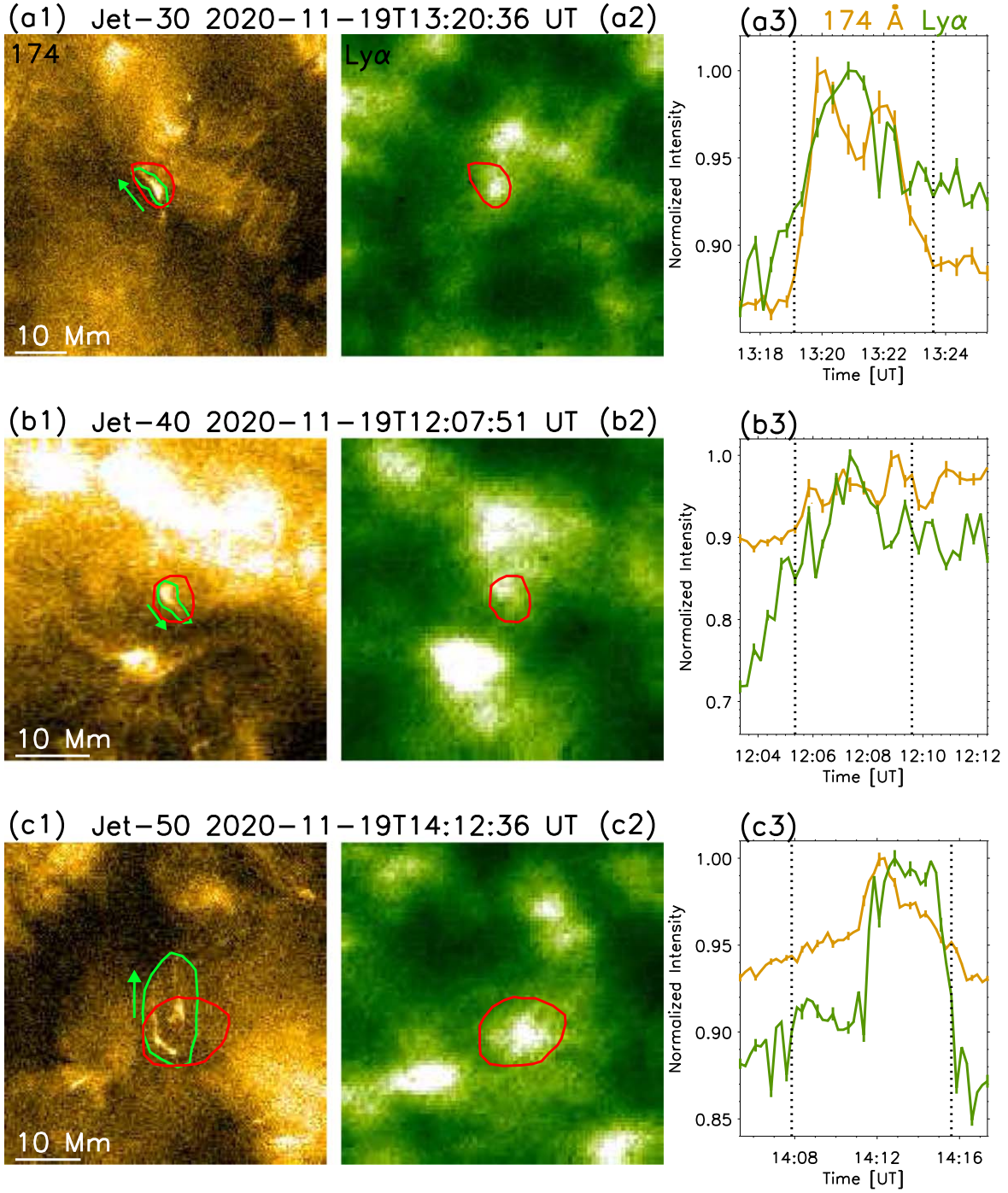
Figure 4. Responses of Jet-30, Jet-40, and Jet-50 in the HRI$_{Ly\alpha}$ images. Left and middle columns: snapshots of three microjets in the HRI$_{EUV}$ and HRI$_{Ly\alpha}$ images. The green contours outline the microjets, and the green arrows represent the propagation directions of the jets. The red contours were used to obtain the average intensity variations at 174 Å and H I Lyα, and the corresponding light curves are shown in the right column. In the right column, the vertical bars indicate the standard errors of the mean values, and the vertical dashed lines represent the starting and ending times of the events.

performed a DEM analysis (Cheung et al. 2015; Su et al. 2018; Xue et al. 2020; Samanta et al. 2021) to investigate their plasma properties with observations in the AIA 94, 131, 171, 193, 211, and 335 Å passbands. As an example, we averaged the intensities within the green contour in Figure 5(b2) and then performed the DEM analysis for Jet-04. We show the temporal evolution of the resultant DEM in Figure 6(a). From 16:09:40 UT to 16:10:20 UT, Jet-04 appears in the AIA EUV passbands and the DEM in the jet region is obviously enhanced in a broad

temperature range of log $(T/K) = 5.65$–6.55. We also calculated its emission-measure (EM)-weighted temperature and obtained a value of log $(T/K) = \sim 6.20$, which is similar to that reported by Paraschiv et al. (2015) using the filter-ratio technique. A similar behavior was also found for other coronal microjets. This indicates the multithermal nature for the plasma in these microjets.

Taking the width (0.4 Mm) of Jet-04 as the LOS integration depth, we can estimate the electron density of
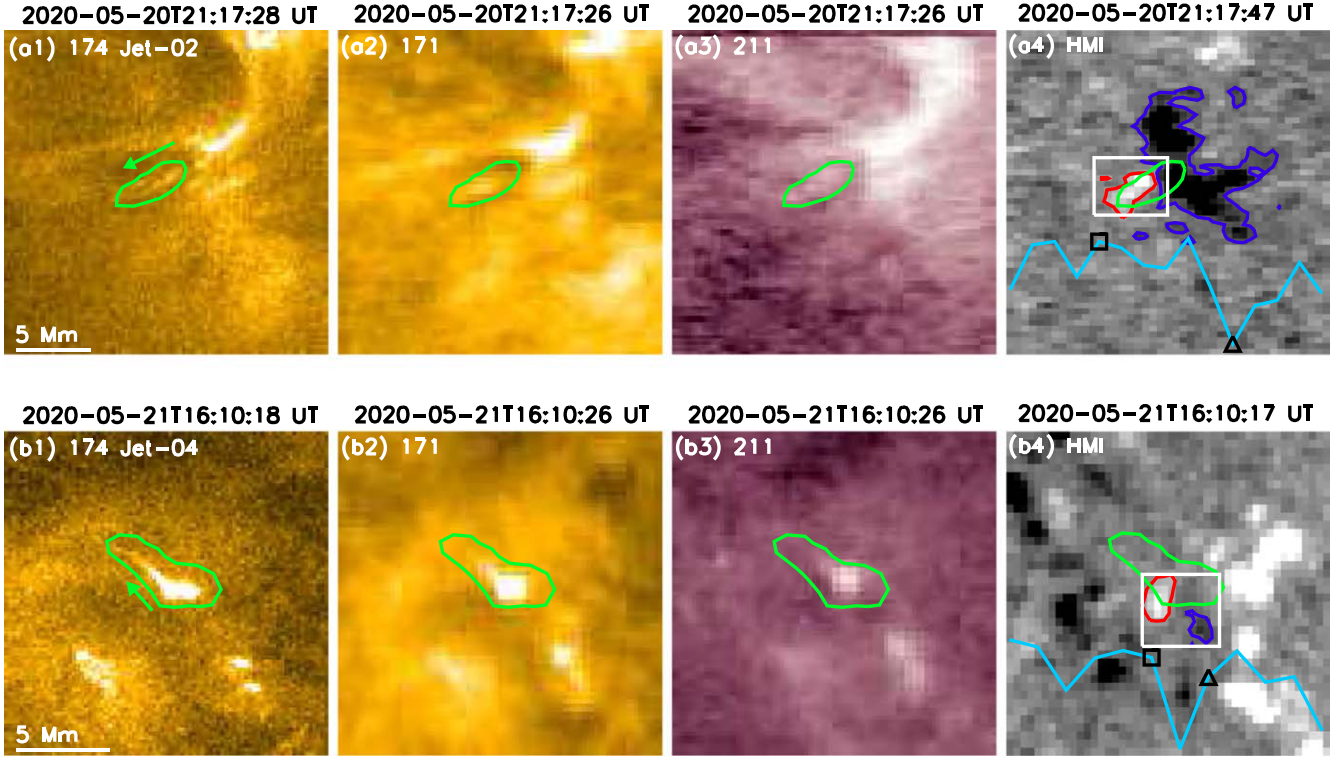
Figure 5. From left to right: images of the HRI$_{EUV}$, AIA 171, 211 Å, and HMI LOS magnetic field for Jet-02 (top row) and Jet-04 (bottom row). The green arrows indicate the propagation directions of the jets. The green contours mark the locations of the microjets. The red and blue contours in (a4) and (b4) represent magnetic field strength with the levels of ± 10 G, respectively. The HMI magnetograms are saturated at ± 50 G. In (a4) and (b4), the overplotted cyan curves show the normalized variations of the minority-polarity (positive for (a4) and negative for (b4)) magnetic fluxes in the white boxes. The black squares and triangles represent the starting and ending times for the events, respectively.
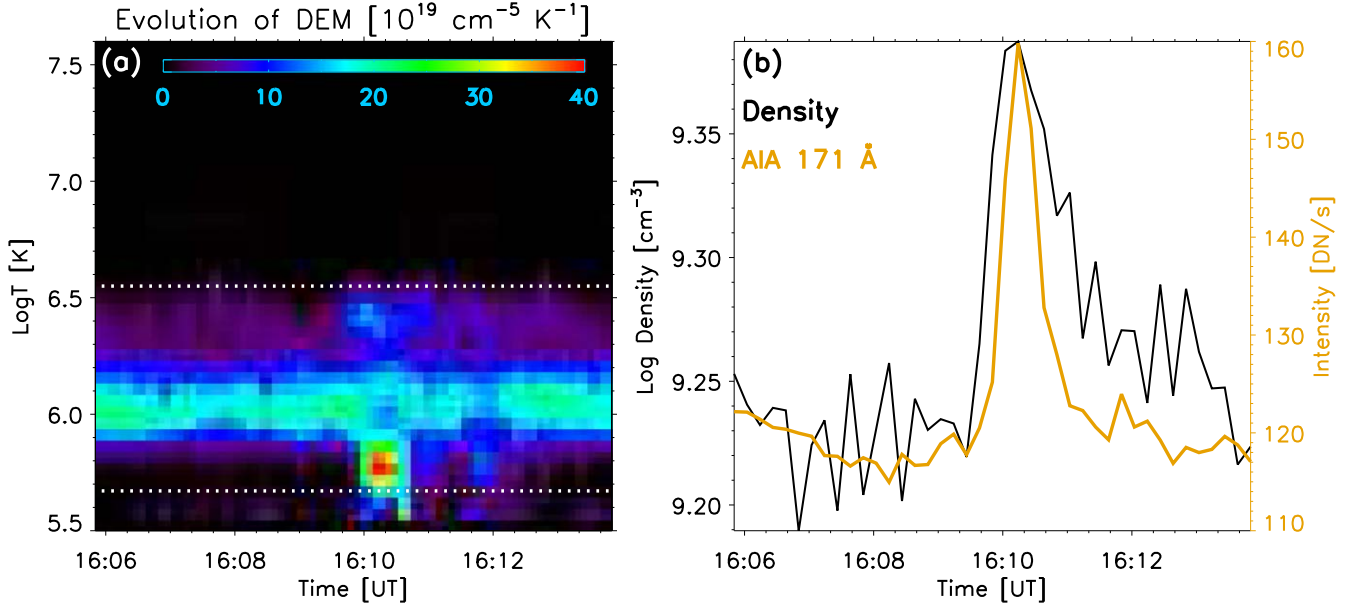
Figure 6. DEM analysis for Jet-04. (a) Evolution of the DEM. The two white dotted lines indicate the temperature range within which the DEM is obviously enhanced when the jet occurs. (b) Temporal evolution of the electron density (black) and AIA 171 Å intensity (yellow) averaged over the green contour in Figure 5(b2).

Jet-04 by integrating the DEM over the temperature range of log $(T/K) = 5.65$–6.55. Figure 6(b) shows the temporal evolution of the density, which closely matches the light curve of the AIA 171 Å intensity. From Figure 6(b), we can see that the density of Jet-04 is $\sim 2.2 \times 10^9 \, \text{cm}^{-3}$.

The densities for other microjets are shown in Table 2. The average density for these quiet-Sun microjets is $\sim 1.4 \times 10^9 \, \text{cm}^{-3}$, which is roughly one order of magnitude lower than the typical density of coronal jets observed in ARs (e.g., Chifor et al. 2008; Tian et al. 2012).

Because we have obtained the physical parameters (spatial scale, projected speed, temperature, density), we can calculate the thermal energy ($E_t = 3N_e k_B TV$) and kinetic energy ($E_k = 0.5 N_e m_p v^2 V$) for the coronal microjets (e.g., Tian et al. 2014a; Chen et al. 2020). Here N_e, m_p, k_B, v, V, and T are the electron number density, proton mass, Boltzmann constant, velocity, volume, and temperature of a microjet. By assuming a coronal microjet with a cylindrical shape (a height of 7.7 Mm and a cross section diameter of 1.0 Mm), a projected speed of 62 km s^{-1}, a mean coronal temperature of 10^6 K, and an electron density of $\sim 1.4 \times 10^9$ cm^{-3}, its thermal and kinetic energies were estimated to be $\sim 3.9 \times 10^{24}$ erg and $\sim 2.9 \times 10^{23}$ erg, respectively. Thus, the total energy of a typical microjet appears to be of the same order of the released energy predicted by the nanoflare theory ($\sim 10^{24}$ erg; Parker 1988).

4. Discussion

At first sight, our microjets appear to be different from the campfires recently discovered from the HRI$_{EUV}$ images. Campfires are characterized by small-scale brightenings in quiet-Sun regions (Berghmans et al. 2021). Most campfires have a loop-like morphology, with a length smaller than 4 Mm and a length to width ratio of 1–5, while the microjets detected here generally have a much larger aspect ratio, 7.7 ± 3.2. The lengths of microjets, 7.7 ± 4.3 Mm, are also considerably larger than those of most campfires. In addition, the microjets are characterized as plasma moving upward from a footpoint brightening, which is not typical for campfires. Another difference is that some coronal microjets also reveal a response in the HRI$_{Ly\alpha}$ images, whereas campfires generally show no signature in Lyα. Nevertheless, we have examined the same data set (data set 3) used by Berghmans et al. (2021) and found that the coronal microjets we identified from data set 3 have also been identified as campfires by the detection method of Berghmans et al. (2021). In several cases, a coronal microjet was identified as sequential campfires or spatially adjacent campfires. Thus, we conclude that the identified coronal microjets are a peculiar subset of coronal campfires. Different from the suggestion that many campfires might correspond to apexes of low-lying small-scale network loops heated at the coronal heights by component reconnection between different loops (Chen et al. 2021), the coronal microjets are more likely to be generated by magnetic reconnection between small-scale magnetic loops and the ambient network field at lower heights.

Another group of small-scale dynamic events resulting from magnetic reconnection are TREEs (e.g., Dere et al. 1991; Innes et al. 1997; Chen & Priest 2006), which are characterized by non-Gaussian line profiles at TR temperatures (e.g., Brueckner & Bartoe 1983; Peter & Brković 2003). Observations have shown that TREEs are usually located at the boundary of magnetic network (e.g., Madjarska & Doyle 2003; Teriaca et al. 2004). Furthermore, they are often associated with jet-like structures (e.g., Huang et al. 2014, 2017; Chen et al. 2019). Here we found that the bases of almost all coronal microjets are located at the network lanes, with many of them at the edges of the lanes. Future investigations are required to understand whether the coronal microjets and TREEs are related.

With AIA observations, Raouafi & Stenborg (2014) reported a new type of coronal jets, called "jetlets," which are smaller than the typical coronal jets. They are often located at the bases of coronal plumes and associated with opposite magnetic polarities (e.g., Pant et al. 2015; Panesar et al. 2018).

Sometimes they can also be identified from the TR images taken by the Interface Region Imaging Spectrograph (IRIS; De Pontieu et al. 2014). These jetlets have an average length of 27 Mm and an average width of 3 Mm, about three times larger than the coronal microjets we report here. More recently, using observation from the High-resolution Coronal Imager 2.1 (Hi-C 2.1; Rachmeler et al. 2019), Panesar et al. (2019) found six smaller jetlet-like structures with an average length of 9 Mm, at edges of network lanes close to an AR. Some of these jetlets appear to be the larger population of TR network jets (Tian et al. 2014b). Some other jetlets might be similar to our quiet-Sun microjets, although our microjets are generally smaller and not associated with coronal plumes. More investigations are required to understand the relationship between the coronal microjets and jetlets. With observations of Hi-C 2.1, Tiwari et al. (2019) recently discovered some fine-scale surge/jet-like features in the core of an AR. Future observations should be performed to examine whether these features are the AR counterpart of our microjets.

Substantial effort has been made to investigate the physical nature and formation mechanisms of solar jets. Magnetic reconnection is generally believed to be the primary cause of solar jets. Numerical simulations of reconnection-driven jets have reproduced many observational features of solar jets. For example, Yokoyama & Shibata (1995) and Yokoyama & Shibata (1996) performed magnetohydrodynamic (MHD) simulations and reproduced both the anemone jets (inverted-Y-shaped jets) and two-sided-loop jets (bidirectional jets). These features, as well as the brightenings caused by plasma heating at the jet footpoints, have also been detected in some of our identified coronal microjets. In reconnection regions, plasma blobs (or plasmoids) can form and move within the jets (e.g., Yokoyama & Shibata 1995, 1996). In a high plasma-β environment, the Kelvin–Helmholtz instability may develop and lead to the formation of vortex-like blobs (Ni et al. 2017; Zhao et al. 2018). On the other hand, the plasmoid instability could occur in the low plasma-β case, and multithermal plasmoid blobs may form and move upward in the jets (Ni et al. 2017). Considering that the corona has a low-β, the moving blobs identified in some microjets are more likely to be plasmoids. The fact that many microjets are associated with mixed-polarity magnetic fluxes and located at the edges of network lanes favors the scenario of jet production by magnetic reconnection between small-scale magnetic loops and the ambient network field in the quiet-Sun regions. This scenario appears to be consistent with that of the simulations performed by Yang et al. (2013) and Yang et al. (2018). In these simulations, magnetic reconnection occurs between closed field and the locally open network field, leading to the generation of an inverted-Y-shaped jet and moving blobs in the simulated jet.

Some of these microjets might also be part of a continuum of jets that emanate from embedded bipoles, i.e., the 3D fan-spine topology, consisting of a minority polarity surrounded by majority-polarity fluxes. This scenario has been extensively studied through observational analysis (e.g., Kumar et al. 2018, 2019a, 2019b) and 3D simulations (e.g., Pariat et al. 2009, 2015, 2016; Wyper & DeVore 2016; Wyper et al. 2016; Karpen et al. 2017; Wyper et al. 2017). Mini-filament eruptions are often involved in this process. For the microjets reported here, no obvious signatures of small-scale (or tiny-, micro-) filaments were observed by the HRI$_{EUV}$ images. However, this

might be due to the fact that the associated filament structures are too small to be resolved by EUI.

Our observations of numerous microjets in quiet-Sun regions might be consistent with the results of Wang et al. (2016), who suggested interchange reconnection as the coronal source of superhalo electrons (Wang et al. 2012). Specifically, they proposed that small-scale interchange reconnections in quiet-Sun regions produce an upward-traveling population of accelerated electrons, which could escape into the interplanetary space and form the superhalo electrons measured in the solar wind.

5. Summary

We have identified 52 coronal microjets from the HRI$_{EUV}$ images taken on six different days. These coronal microjets appear as quasi-collimated plasma ejections from clear brightenings in the quiet-Sun regions. Some of these microjets reveal an inverted-Y shape and include moving blobs, which are similar to many previously known jets. The footpoints of most microjets are located at the edges of network lanes and associated with mixed-polarity magnetic fluxes. These observational features suggest that the coronal microjets are the small-scale version of coronal jets, which are likely generated by magnetic reconnection between small-scale magnetic loops and the ambient network field in the quiet-Sun regions.

We have measured various physical parameters of the coronal microjets, and found that (1) the durations are mostly a few minutes, (2) the projected speeds are mostly 40–90 km s^{-1}, (3) the average lengths and width are $\sim$7.7 Mm and $\sim$1.0 Mm, respectively, and (4) the aspect ratios of the jets are generally 4–13. We have examined the response of the coronal microjets in the HRI$_{Ly\alpha}$ images and found that 11 out of 30 jets show a response, possibly indicating the generation of these 11 microjets at lower heights compared to others. When the AIA data are available, we found that almost all of the microjets have signatures in the AIA EUV passbands, especially in the 304, 171, 193, and 211 Å passbands. Through a DEM analysis, we found that these coronal microjets are multithermal, and their average density is $\sim$1.4 $\times$ 10^9 cm^{-3}. The thermal and kinetic energies of these coronal microjets were estimated to be $\sim$3.9 $\times$ 10^{24} erg and $\sim$2.9 $\times$ 10^{23} erg, respectively, which fall into the energy range of coronal nanoflares.

ORCID iDs

Zhenyong Hou ⓘ https://orcid.org/0000-0003-4804-5673
Hui Tian ⓘ https://orcid.org/0000-0002-1369-1758
Hechao Chen ⓘ https://orcid.org/0000-0001-7866-4358
Yajie Chen ⓘ https://orcid.org/0000-0001-5494-4339
Jiansen He ⓘ https://orcid.org/0000-0001-8179-417X
Linghua Wang ⓘ https://orcid.org/0000-0001-7309-4325
Xianyong Bai ⓘ https://orcid.org/0000-0003-2686-9153

References

Antolin, P., Pagano, P., Testa, P., Petralia, A., & Reale, F. 2021, NatAs, 5, 54
Bai, X., Socas-Navarro, H., Nóbrega-Siverio, D., et al. 2019, ApJ, 870, 90
Berghmans, D., Auchère, F., Long, D. M., et al. 2021, A&A, arXiv:2104.03382
Bharti, L., Solanki, S. K., & Hirzberger, J. 2017, A&A, 597, A127
Brueckner, G. E., & Bartoe, J. D. F. 1983, ApJ, 272, 329
Chandrashekhar, K., Bemporad, A., Banerjee, D., Gupta, G. R., & Teriaca, L. 2014a, A&A, 561, A104
Chandrashekhar, K., Morton, R. J., Banerjee, D., & Gupta, G. R. 2014b, A&A, 562, A98
Chen, H., Zhang, J., De Pontieu, B., et al. 2020, ApJ, 899, 19
Chen, H., Zhang, J., Ma, S., Yan, X., & Xue, J. 2017a, ApJL, 841, L13
Chen, H. D., Jiang, Y. C., & Ma, S. L. 2008, A&A, 478, 907
Chen, J., Su, J., Deng, Y., & Priest, E. R. 2017b, ApJ, 840, 54
Chen, J., Su, J., Yin, Z., et al. 2015, ApJ, 815, 71
Chen, P. F., & Priest, E. R. 2006, SoPh, 238, 313
Chen, Y., Przybylski, D., Peter, H., et al. 2021, A&A, in press
Chen, Y., Tian, H., Huang, Z., Peter, H., & Samanta, T. 2019, ApJ, 873, 79
Cheung, M. C. M., Boerner, P., Schrijver, C. J., et al. 2015, ApJ, 807, 143
Chifor, C., Young, P. R., Isobe, H., et al. 2008, A&A, 481, L57
Cirtain, J. W., Golub, L., Lundquist, L., et al. 2007, Sci, 318, 1580
Culhane, L., Harra, L. K., Baker, D., et al. 2007, PASJ, 59, S751
de Pontieu, B., McIntosh, S., Hansteen, V. H., et al. 2007, PASJ, 59, S655
De Pontieu, B., McIntosh, S. W., Carlsson, M., et al. 2011, Sci, 331, 55
De Pontieu, B., Title, A. M., Lemen, J. R., et al. 2014, SoPh, 289, 2733
Dere, K. P., Bartoe, J. D. F., Brueckner, G. E., Ewing, J., & Lund, P. 1991, JGR, 96, 9399
He, J. S., Marsch, E., Curdt, W., et al. 2010, A&A, 519, A49
Hong, J., Jiang, Y., Yang, J., et al. 2016, ApJ, 830, 60
Hou, Y., Zhang, J., Li, T., Yang, S., & Li, X. 2017, ApJL, 848, L9
Hou, Y. J., Li, T., Zhong, S. H., et al. 2020, A&A, 642, A44
Huang, Z., Madjarska, M. S., Scullion, E. M., et al. 2017, MNRAS, 464, 1753
Huang, Z., Madjarska, M. S., Xia, L., et al. 2014, ApJ, 797, 88
Innes, D. E., Inhester, B., Axford, W. I., & Wilhelm, K. 1997, Natur, 386, 811
Jiang, Y. C., Chen, H. D., Li, K. J., Shen, Y. D., & Yang, L. H. 2007, A&A, 469, 331
Karpen, J. T., DeVore, C. R., Antiochos, S. K., & Pariat, E. 2017, ApJ, 834, 62
Katsukawa, Y., Berger, T. E., Ichimoto, K., et al. 2007, Sci, 318, 1594
Kumar, P., Karpen, J. T., Antiochos, S. K., et al. 2018, ApJ, 854, 155
Kumar, P., Karpen, J. T., Antiochos, S. K., et al. 2019b, ApJ, 873, 93
Kumar, P., Karpen, J. T., Antiochos, S. K., Wyper, P. F., & DeVore, C. R. 2019a, ApJL, 885, L15
Lemen, J. R., Title, A. M., Akin, D. J., et al. 2012, SoPh, 275, 17
Li, D., Ning, Z., & Su, Y. 2016, Ap&SS, 361, 301
Li, X., Zhang, J., Yang, S., & Hou, Y. 2019, PASJ, 71, 14
Liu, J., Fang, F., Wang, Y., et al. 2016, ApJ, 817, 126
Madjarska, M. S. 2019, LRSP, 16, 2
Madjarska, M. S., & Doyle, J. G. 2003, A&A, 403, 731
Moore, R. L., Cirtain, J. W., Sterling, A. C., & Falconer, D. A. 2010, ApJ, 720, 757
Moore, R. L., Sterling, A. C., & Panesar, N. K. 2018, ApJ, 859, 3
Mulay, S. M., Tripathi, D., Del Zanna, G., & Mason, H. 2016, A&A, 589, A79
Müller, D., St., Cyr, O. C., Zouganelis, I., et al. 2020, A&A, 642, A1
Narang, N., Arbacher, R. T., Tian, H., et al. 2016, SoPh, 291, 1129
Ni, L., Ji, H., Murphy, N. A., & Jara-Almonte, J. 2020, RSPSA, 476, 20190867
Ni, L., Zhang, Q.-M., Murphy, N. A., & Lin, J. 2017, ApJ, 841, 27
Nisticò, G., Bothmer, V., Patsourakos, S., & Zimbardo, G. 2009, SoPh, 259, 87
Panesar, N. K., Sterling, A. C., Moore, R. L., et al. 2018, ApJL, 868, L27
Panesar, N. K., Sterling, A. C., Moore, R. L., et al. 2019, ApJL, 887, L8
Panesar, N. K., Sterling, A. C., Moore, R. L., & Chakrapani, P. 2016, ApJL, 832, L7
Pant, V., Dolla, L., Mazumder, R., et al. 2015, ApJ, 807, 71
Paraschiv, A. R., Bemporad, A., & Sterling, A. C. 2015, A&A, 579, A96

Paraschiv, A. R., Donea, A., & Leka, K. D. 2020, ApJ, 891, 149
Pariat, E., Antiochos, S. K., & DeVore, C. R. 2009, ApJ, 691, 61
Pariat, E., Dalmasse, K., DeVore, C. R., Antiochos, S. K., & Karpen, J. T. 2015, A&A, 573, A130
Pariat, E., Dalmasse, K., DeVore, C. R., Antiochos, S. K., & Karpen, J. T. 2016, A&A, 596, A36
Parker, E. N. 1988, ApJ, 330, 474
Pesnell, W. D., Thompson, B. J., & Chamberlin, P. C. 2012, SoPh, 275, 3
Peter, H., & Brković, A. 2003, A&A, 403, 287
Qi, Y., Huang, Z., Xia, L., et al. 2019, SoPh, 294, 92
Rachmeler, L. A., Winebarger, A. R., Savage, S. L., et al. 2019, SoPh, 294, 174
Raouafi, N. E., Patsourakos, S., Pariat, E., et al. 2016, SSRv, 201, 1
Raouafi, N. E., & Stenborg, G. 2014, ApJ, 787, 118
Rochus, P., Auchère, F., Berghmans, D., et al. 2020, A&A, 642, A8
Rouppe van der Voort, L., De Pontieu, B., Pereira, T. M. D., Carlsson, M., & Hansteen, V. 2015, ApJL, 799, L3
Sakaue, T., Tei, A., Asai, A., et al. 2017, PASJ, 69, 80
Samanta, T., Tian, H., Chen, B., et al. 2021, The Innovation, 2, 100083
Samanta, T., Tian, H., Yurchyshyn, V., et al. 2019, Sci, 366, 890
Savcheva, A., Cirtain, J., Deluca, E. E., et al. 2007, PASJ, 59, S771
Scherrer, P. H., Schou, J., Bush, R. I., et al. 2012, SoPh, 275, 207
Shen, Y. 2021, RSPSA, 477, 20200217
Shen, Y., Liu, Y., Liu, Y. D., et al. 2018, ApJ, 861, 105
Shen, Y., Liu, Y., Su, J., & Deng, Y. 2012, ApJ, 745, 164
Shibata, K., Nakamura, T., Matsumoto, T., et al. 2007, Sci, 318, 1591
Shimojo, M., Hashimoto, S., Shibata, K., et al. 1996, PASJ, 48, 123
Shimojo, M., & Shibata, K. 2000, ApJ, 542, 1100
Srivastava, A. K., Erdélyi, R., Murawski, K., & Kumar, P. 2012, SoPh, 281, 729
Srivastava, A. K., & Murawski, K. 2011, A&A, 534, A62
Sterling, A. C., Harra, L. K., Moore, R. L., & Falconer, D. A. 2019, ApJ, 871, 220
Sterling, A. C., & Hudson, H. S. 1997, ApJL, 491, L55
Sterling, A. C., Moore, R. L., Falconer, D. A., et al. 2016, ApJ, 821, 100

Sterling, A. C., Moore, R. L., Falconer, D. A., & Adams, M. 2015, Natur, 523, 437
Su, Y., Veronig, A. M., Hannah, I. G., et al. 2018, ApJL, 856, L17
Teriaca, L., Banerjee, D., Falchi, A., Doyle, J. G., & Madjarska, M. S. 2004, A&A, 427, 1065
Tian, H., DeLuca, E. E., Cranmer, S. R., et al. 2014b, Sci, 346, 1255711
Tian, H., Kleint, L., Peter, H., et al. 2014a, ApJL, 790, L29
Tian, H., McIntosh, S. W., Xia, L., He, J., & Wang, X. 2012, ApJ, 748, 106
Tian, H., Yurchyshyn, V., Peter, H., et al. 2018, ApJ, 854, 92
Tian, Z., Liu, Y., Shen, Y., et al. 2017, ApJ, 845, 94
Tiwari, S. K., Moore, R. L., Winebarger, A. R., & Alpert, S. E. 2016, ApJ, 816, 92
Tiwari, S. K., Panesar, N. K., Moore, R. L., et al. 2019, ApJ, 887, 56
Wang, L., Lin, R. P., Salem, C., et al. 2012, ApJL, 753, L23
Wang, W., Wang, L., Krucker, S., & Hannah, I. 2016, SoPh, 291, 1357
Wang, Y., Zhang, Q., & Ji, H. 2021, ApJ, 913, 59
Wei, H., Huang, Z., Hou, Z., et al. 2020, MNRAS, 498, L104
Wyper, P. F., Antiochos, S. K., & DeVore, C. R. 2017, Natur, 544, 452
Wyper, P. F., & DeVore, C. R. 2016, ApJ, 820, 77
Wyper, P. F., DeVore, C. R., Karpen, J. T., & Lynch, B. J. 2016, ApJ, 827, 4
Xing, C., Cheng, X., & Ding, M. D. 2020, The Innovation, 1, 100059
Xue, J., Su, Y., Li, H., & Zhao, X. 2020, ApJ, 898, 88
Yang, L., He, J., Peter, H., et al. 2013, ApJ, 777, 16
Yang, L., Peter, H., He, J., et al. 2018, ApJ, 852, 16
Yang, L., Yan, X., Xue, Z., et al. 2019, ApJ, 887, 239
Yang, L.-H., Jiang, Y.-C., Yang, J.-Y., et al. 2011, RAA, 11, 1229
Yokoyama, T., & Shibata, K. 1995, Natur, 375, 42
Yokoyama, T., & Shibata, K. 1996, PASJ, 48, 353
Zhang, Q. M., & Ji, H. S. 2014, A&A, 567, A11
Zhang, Q. M., Ji, H. S., & Su, Y. N. 2016, SoPh, 291, 859
Zhao, T.-L., Ni, L., Lin, J., & Ziegler, U. 2018, RAA, 18, 045
Zheng, R., Chen, Y., Huang, Z., et al. 2018, ApJ, 861, 108
Zhu, X., Wang, H., Cheng, X., & Huang, C. 2017, ApJL, 844, L20